



Publication Year	2017
Acceptance in OA @INAF	2020-08-27T14:24:58Z
Title	A Universal Transition in Atmospheric Diffusion for Hot Subdwarfs Near 18,000 K
Authors	Brown, T. M.; Taylor, J. M.; CASSISI, Santi; Sweigart, A. V.; Bellini, A.; et al.
DOI	10.3847/1538-4357/aa9ce3
Handle	http://hdl.handle.net/20.500.12386/26896
Journal	THE ASTROPHYSICAL JOURNAL
Number	851



A Universal Transition in Atmospheric Diffusion for Hot Subdwarfs Near 18,000 K*

T. M. Brown¹ , J. M. Taylor¹, S. Cassisi² , A. V. Sweigart³, A. Bellini¹ , L. R. Bedin⁴,
M. Salaris⁵, A. Renzini⁴, and E. Dalessandro⁶

¹ Space Telescope Science Institute, 3700 San Martin Drive, Baltimore, MD 21218, USA; tbrown@stsci.edu, bellini@stsci.edu, jotaylor@stsci.edu

² INAF, Osservatorio Astronomico d’Abruzzo, Via Mentore Maggini s.n.c., I-64100 Teramo, Italy; cassisi@oa-teramo.inaf.it

³ NASA Goddard Space Flight Center, Greenbelt, MD 20771, USA; allen.sweigart@gmail.com

⁴ INAF, Osservatorio Astronomico di Padova, Vicolo dell’Osservatorio 5, I-35122 Padova, Italy; luigi.bedin@oapd.inaf.it, alvio.renzini@oapd.inaf.it

⁵ Astrophysics Research Institute, Liverpool John Moores University, Liverpool Science Park, IC2 Building, 146 Brownlow Hill, Liverpool L3 5RF, UK; M.Salaris@ljmu.ac.uk

⁶ INAF, Osservatorio Astronomico di Bologna, Via Gobetti 93/3, I-40129, Bologna, Italy; emanuele.dalessandro@oabo.inaf.it

Received 2017 October 25; revised 2017 November 21; accepted 2017 November 21; published 2017 December 19

Abstract

In the color–magnitude diagrams of globular clusters, when the locus of stars on the horizontal branch extends to hot temperatures, discontinuities are observed at colors corresponding to $\sim 12,000$ and $\sim 18,000$ K. The former is the “Grundahl jump” that is associated with the onset of radiative levitation in the atmospheres of hot subdwarfs. The latter is the “Momany jump” that has remained unexplained. Using the Space Telescope Imaging Spectrograph on the *Hubble Space Telescope*, we have obtained ultraviolet and blue spectroscopy of six hot subdwarfs straddling the Momany jump in the massive globular cluster ω Cen. By comparison to model atmospheres and synthetic spectra, we find that the feature is due primarily to a decrease in atmospheric Fe for stars hotter than the feature, amplified by the temperature dependence of the Fe absorption at these effective temperatures.

Key words: globular clusters: general – globular clusters: individual (NGC 5139) – stars: atmospheres – stars: evolution – stars: horizontal-branch – ultraviolet: stars

1. Introduction

The well-behaved luminosity of the horizontal branch (HB) makes it an important standard candle in old populations (e.g., Carretta et al. 2000). However, the HB locus exhibits many morphological peculiarities that have been the subject of study for decades. These include the “second parameter” debate over the factors driving the HB color distribution (see Catelan 2009 for a review), overluminous HB stars in He-enhanced populations (e.g., Busso et al. 2007; Caloi & D’Antona 2007), subluminous HB stars beyond the hot end of the standard HB sequence (D’Cruz et al. 1996, 2000; Brown et al. 2001), and luminosity jumps within the HB distribution (Grundahl et al. 1998, 1999; Momany et al. 2002, 2004). Even the existence of the HB itself, representing a range in envelope mass for an approximately constant core mass, is a reminder of one of astronomy’s mysteries—the dispersion in mass loss occurring on the red giant branch.

The *Hubble Space Telescope* (HST) UV Legacy Survey of Galactic Globular Clusters treasury program (Piotto et al. 2015) enabled a new investigation of these phenomena by providing a large and homogeneous catalog of UV and blue photometry for over 50 globular clusters. The primary goal of the program was an investigation of the multiple populations phenomenon in globular clusters. The bandpasses for the program are sensitive to abundance variations in cool stars, allowing these distinct populations to be cleanly separated and characterized (e.g., Milone et al. 2017a). A secondary goal of the program was a characterization of the hot subdwarfs in these clusters. Brown

et al. (2016) used this dataset to explore the “Grundahl jump” (hereafter G-jump; Grundahl et al. 1998, 1999) and “Momany jump” (hereafter M-jump; Momany et al. 2002, 2004) that appear as discontinuities within the HB distribution near effective temperatures of $\sim 12,000$ and $\sim 18,000$ K (Figure 1). In the color–color plane of Figure 1, the stars between the G-jump and M-jump appear to deviate from the expected location of the theoretical zero-age HB (see Figures 6 and 7 in Brown et al. 2016). They found that the G-jump falls at a consistent temperature for 31 of the 33 survey clusters where it is populated; the only exceptions are NGC 6388 and NGC 6441, two metal-rich clusters greatly enhanced in helium. The G-jump is associated with the onset of radiative levitation for metals and the gravitational settling of helium in the atmospheres of subdwarfs hotter than the G-jump (Moehler et al. 1999, 2000; Behr 2003; Pace et al. 2006). Brown et al. (2016) explained that the hotter G-jump in NGC 6388 and NGC 6441 is likely associated with helium enhancement because it shifts the onset of surface convection to higher effective temperatures. They also found that the M-jump is at a consistent temperature for all 15 of the survey clusters where it is populated, including the clusters NGC 6388 and NGC 6441. Given the variety of cluster parameters in this set (e.g., mass, metallicity, and helium abundance), the consistency of the M-jump demonstrates that it is clearly a universal atmospheric phenomenon (like the G-jump). However, with only broadband photometry, it was not possible to determine the atmospheric changes associated with the feature.

To further investigate the nature of the M-jump, we obtained HST spectroscopy of hot subdwarfs straddling the feature in the massive globular cluster ω Cen (Figure 1). One may wonder why we chose such an unusual cluster—the most massive in the Galaxy, and a striking example of the multiple populations phenomenon in globular clusters, with variations in the light

* Based on observations made with the NASA/ESA *Hubble Space Telescope*, obtained at the Space Telescope Science Institute, which is operated by the Association of Universities for Research in Astronomy, Inc., under NASA contract NAS 5-26555. These observations are associated with program GO-14759.

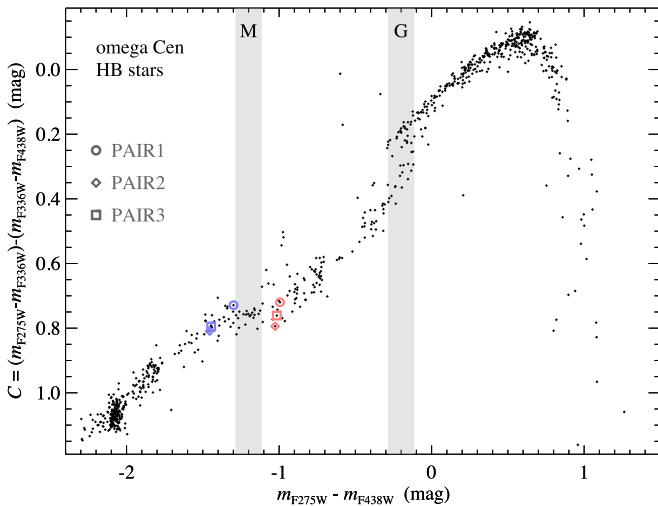


Figure 1. WFC3 photometry (*black points*) of HB stars in ω Cen (Bellini et al. 2017a), shown as a color–color diagram that makes it easy to discern the G-jump and M-jump (labeled; as in Brown et al. 2016). The ordinate is a color index (C) that is useful for discerning changes in the stellar atmosphere (in the hot stars here but also the cooler stars studied in the multiple populations phenomenon). For our investigation, we obtained STIS near-UV (G230L) and blue (G430L) spectroscopy of six stars (colored symbols matching those in Figure 2) that straddle the M-jump, with wavelength coverage that includes the three photometric bands employed in this color–color diagram (F275W, F336W, and F438W). If the photometry here is aligned to a theoretical zero-age HB locus (see Brown et al. 2016), the gray band representing the M-jump spans $\sim 15,000$ – $18,000$ K in effective temperature.

elements and iron (e.g., Marino et al. 2011; Bellini et al. 2017b). First, it is worth noting that the hot HB stars are preferentially drawn from a subset of the ω Cen populations—the bluest of the multiple main sequences (see Cassisi et al. 2009). That said, even with the cluster’s distinct sub-populations, the cluster’s composite population is better constrained than that of an assorted collection of field subdwarfs. More importantly, Brown et al. (2016) demonstrated that the G-jump and M-jump are the products of stellar atmosphere transitions instead of population distinctions; the transition responsible for the G-jump can be shifted to a hotter effective temperature at extreme He abundance, but the M-jump is constant even in the presence of such He enhancements. For these reasons, the peculiar populations of ω Cen are not a concern for this study. The main motivation for targeting ω Cen is that it offers a large sample of relatively nearby stars straddling the M-jump, with a level of crowding that enables clean spectroscopy with the Space Telescope Imaging Spectrograph (STIS) aboard the *HST*. In this paper, we analyze the spectra of six stars (three on each side of the M-jump) to characterize the atmospheric transitions responsible for the feature.

2. Data

Our program obtained six orbits of *HST*/STIS spectroscopy in ω Cen, with one orbit of near-UV (G230L) and one orbit of blue (G430L) exposures at each of the three slit positions (Figure 2). Each position of the $52'' \times 0.5''$ slit was chosen to sample a pair of stars straddling the M-jump in ω Cen (Figure 1 and Table 1); note that the slit spans $52''$ in the G430L exposures, but is limited by the detector to $25''$ in the G230L exposures. The placement of each stellar pair along the slit

Table 1
Targets

Name	R.A. (J2000)	Decl. (J2000)	$m_{F275W} - m_{F438W}$ (mag)	C (mag)
Blue 1	13 26 36.45	−47 28 28.54	−1.30	0.73
Red 1	13 26 36.76	−47 28 24.49	−0.99	0.72
Blue 2	13 26 48.23	−47 30 32.35	−1.46	0.81
Red 2	13 26 48.70	−47 30 37.56	−1.03	0.79
Blue 3	13 26 47.90	−47 29 00.64	−1.45	0.80
Red 3	13 26 47.08	−47 29 12.47	−1.02	0.76

midline was facilitated by archival *HST* imaging (providing excellent relative astrometry) and acquisition on a bright isolated star (placing the relative astrometry in an absolute frame). For each slit position, three individual exposures were obtained for each of the two gratings (G230L and G430L), with dithering along the slit to enable the removal of detector artifacts. A link to the data is provided here: doi:10.17909/T9BT2R.

The STIS pipeline provides a variety of corrections (see Bostroem & Proffitt 2011), but the reduction steps for the near-UV and blue spectroscopy are somewhat distinct, given the different detectors involved. G430L data are obtained with the STIS charge coupled device, which has suffered considerable radiation damage during its 20 years in flight. This damage has reduced the charge transfer efficiency (CTE) and greatly increased the number of hot pixels. To account for these issues, we processed the data with contemporaneous darks and biases, and then performed a pixel-based correction for CTE losses using the STIS_CTI routine, which is based on the algorithms used on the *HST* imaging instruments (Anderson & Bedin 2010). The resulting frames were shifted to a common position (accounting for the dithers along the slit) and combined with the masking of cosmic rays, hot pixels, and dead pixels. The blue spectra were then extracted with the X1D routine in the STISTOOLS software package. G230L data are obtained with a STIS multi-anode multi-channel array, where CTE is not an issue, there is little sensitivity to cosmic rays, and the evolution in defective pixels is much slower over time. The data were dark and bias corrected, shifted to a common frame, combined with the masking of defective pixels, and extracted with the X1D routine. The near-UV and blue spectroscopy were then combined into a single spectrum after normalizing to a common level (a correction of less than 5%), using a clean wavelength region 10 nm wide. The final spectra of our stars are shown in Figure 3. The naming convention for our targets is straightforward: there are three slit positions, and each position has a pair of red and blue stars, so each name gives the color and slit position (e.g., Blue 2 is the blue star in the pair at slit position 2).

3. Analysis

To ease comparisons, we first compare each of the spectra to that of Blue 1 (Figure 3). Not surprisingly, all of the red stars have spectral slopes redder than that of Blue 1 (or any of the blue stars). Photometry of our targets (Figure 1; Bellini et al. 2017a) had already implied that the blue stars in our sample are 2000–4000 K hotter than the red stars, if one folds synthetic spectra at the cluster metallicity through the WFC3 bandpasses. However, the Balmer jump in these red stars is not significantly stronger than that in the

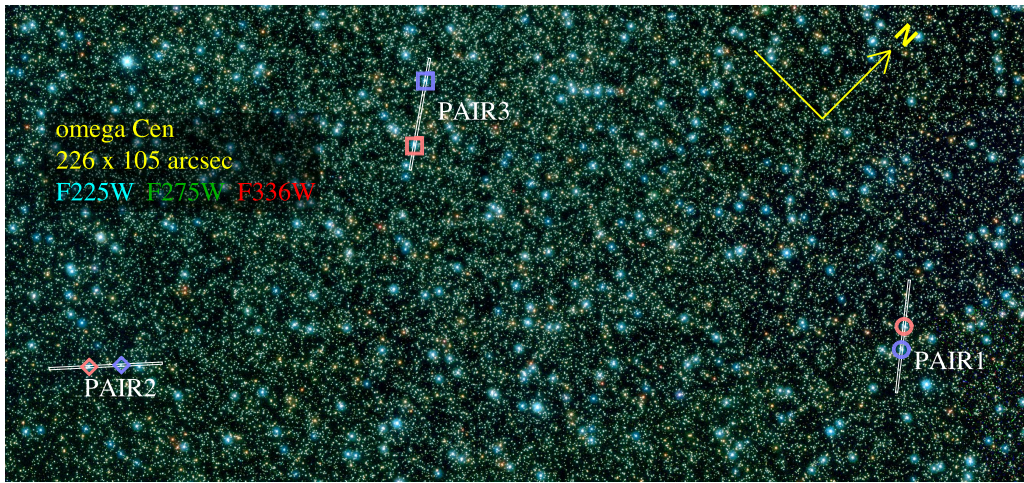


Figure 2. False-color image of our field, constructed from three ultraviolet bands of WFC3 imaging to highlight the hottest stars: F225W (blue), F275W (green), and F336W (red). The images come from an *HST* calibration program (program 11452; PI: Quijano). Note that Brown et al. (2016) explored HB discontinuities with the F275W, F336W, and F438W filters, which motivated the wavelength coverage obtained in our spectroscopy here. A $25'' \times 0''.5$ box indicates the three positions of the STIS slit in our program. At each slit position, a star redward of the M-jump and a star blueward of the M-jump were placed within the slit (colored symbols matching those in Figure 1). In this paper, targets are designated by the slit position and this relative color (e.g., Blue 2 is the blue star in the pair at slit position 2).

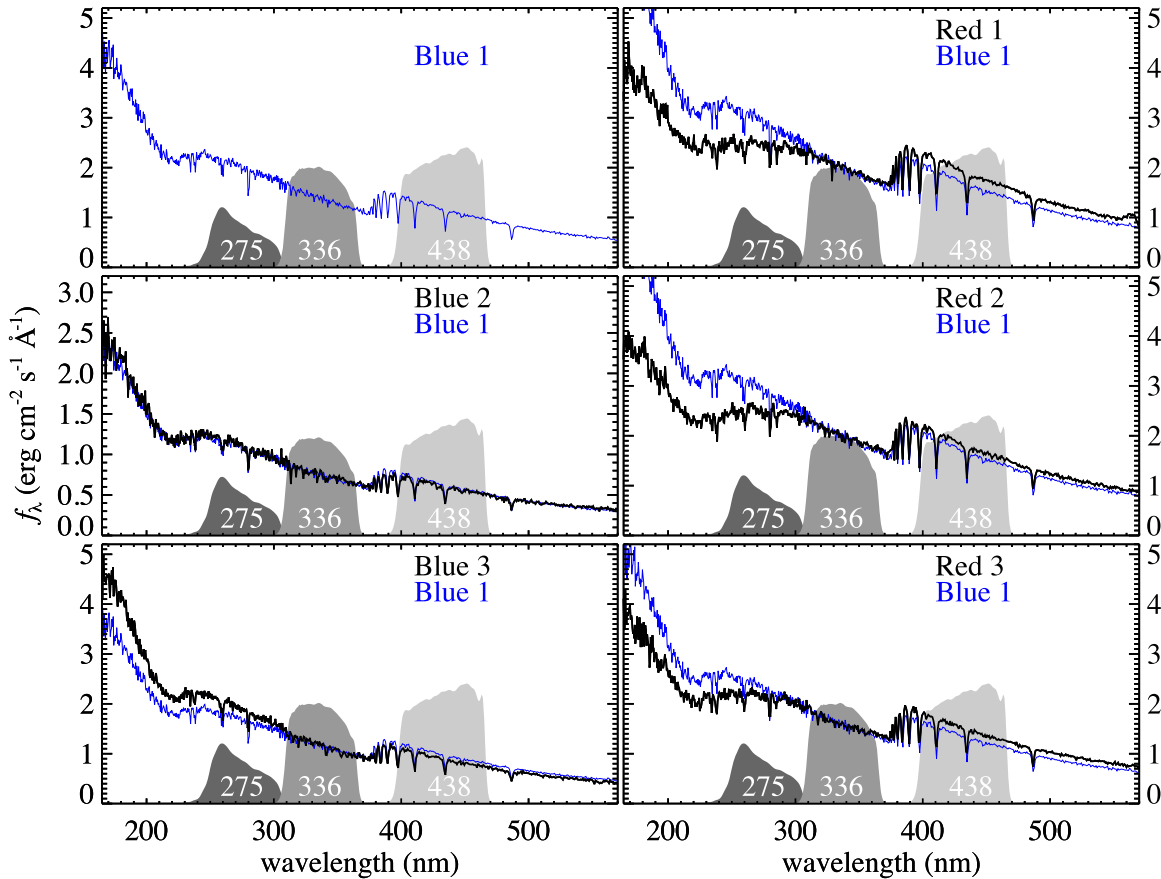


Figure 3. Spectra for each of the six stars in our analysis (black curves). The spectrum of Blue 1 (blue curves) is overplotted in each panel, normalized at 310–360 nm (i.e., F336W) to ease comparisons between the spectra. We also show the bandpasses of the WFC3 filters (gray shading; arbitrary normalization) used in the color-color diagram that drove our investigation (Figure 1).

blue stars, in contradiction of expectations if the stars have the same chemical composition. This is clearer if we look at the ratio of flux for each star against the flux of Blue 1 (Figure 4). None of the flux ratios for the red stars show a significant break at the Balmer jump. Assuming the red stars are truly cooler than the blue stars, the Balmer jump in the red stars may be diminished if the

red stars have higher atmospheric metallicities than those of the blue stars (Figure 5). This is our first indication of a distinction in atmospheric abundances between the groups of stars on either side of the M-jump.

The M-jump was originally discovered (Momany et al. 2002) and explored (Momany et al. 2004) using *U*-band

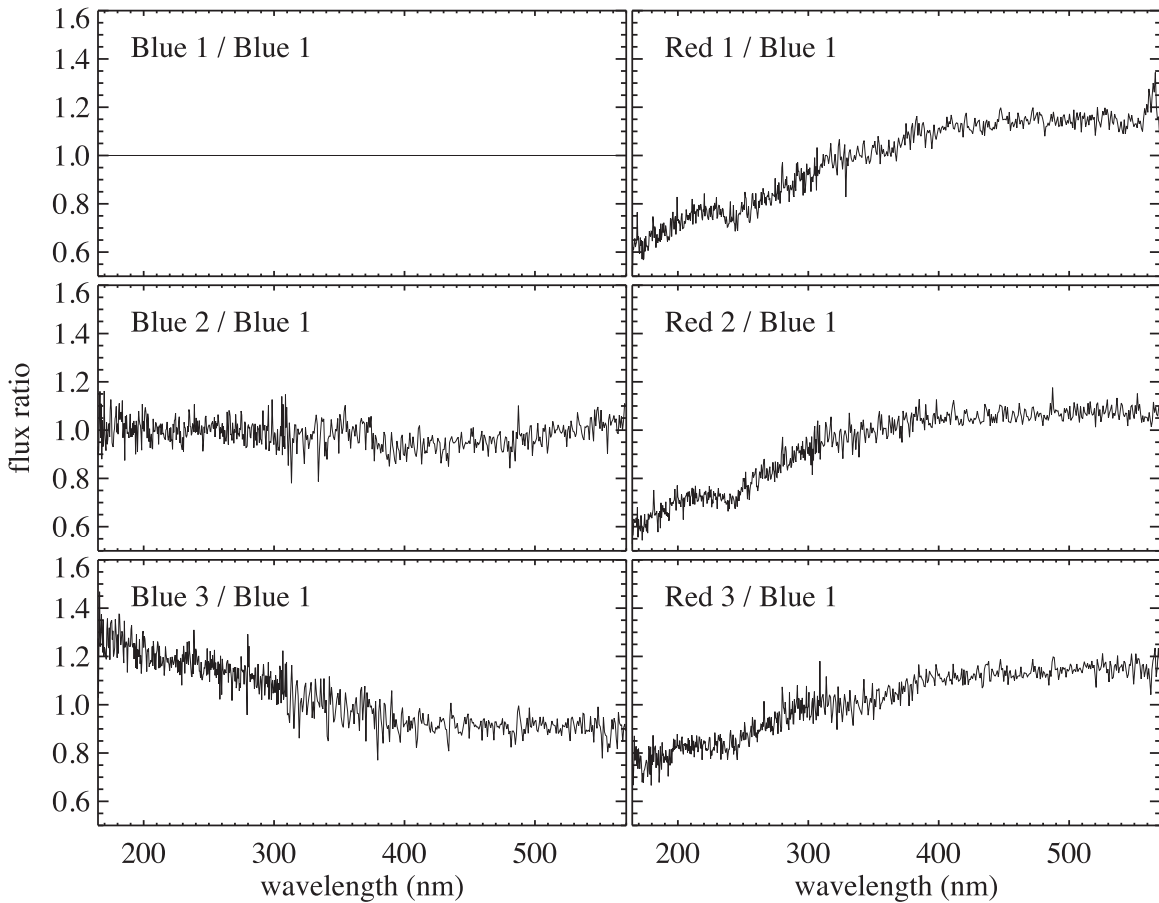


Figure 4. Flux ratio of each spectrum to that of Blue 1, normalized to unity over 310–360 nm (i.e., the F336W bandpass, and just blueward of the Balmer jump). The photometry of the red stars implies they have effective temperatures 2000–4000 K cooler than those of the blue stars. With that temperature difference, one expects the red stars to have significantly redder slopes in this wavelength range (as evident in the right panels), but also significantly stronger Balmer jumps. Instead, the flux ratio of each red star to Blue 1 is surprisingly continuous across 365 nm. A change in overall continuum slope without a change in Balmer jump strength implies that the red stars have atmospheric metallicities that are significantly higher than those of the blue stars (see Figure 5).

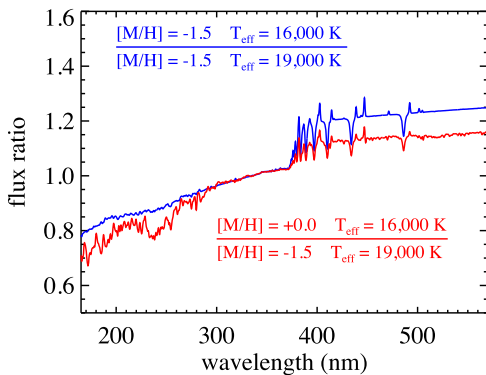


Figure 5. The flux ratio of a 16,000 K star to a 19,000 K star (blue curve) exhibits a clear break at the Balmer jump when both stars are at the same metallicity. When the atmospheric metallicity of the cooler star is elevated relative to that of the hotter star, the distinction in Balmer jump strength is reduced (red curve).

photometry. The feature is more easily seen in the color–color diagrams of Brown et al. (2016; Figure 1), which also employ a band (F336W) approximating the U -band. The phenomenon must produce spectral features that affect the U -band itself or the strength of the U -band relative to neighboring bandpasses. If one considers the stars lying immediately to the red side of the M-jump in Figure 1, the photometric deviation could be due to these stars having $m_{F275W} - m_{F336W}$ colors that are too red,

$m_{F336W} - m_{F438W}$ colors that are too blue, or a combination thereof. The spectra in Figure 3 imply that it is indeed due to both effects: the red stars are much redder in $m_{F275W} - m_{F336W}$ color than the blue stars, but the weaker-than-expected Balmer jumps in the red stars make their $m_{F336W} - m_{F438W}$ colors bluer than they would be otherwise.

To further constrain the properties of the stars straddling the M-jump, we turn to fits of synthetic spectra to the data. We begin with the Castelli & Kurucz (2003) grid of synthetic spectra. This grid is unlikely to satisfactorily reproduce the spectra of hot subdwarfs, because it assumes the abundances scale together (either at scaled solar abundance or with α -element enhancement), while hot subdwarfs exhibit significant atmospheric abundance anomalies caused by atmospheric diffusion. Nevertheless, the grid serves as a starting point.

There are two unknowns of interest: the effective temperature and abundance. We cannot perform a single-parameter fit of the abundance, because we have no independent measure of the effective temperature; the photometry only allows an estimate of the effective temperature given an assumed abundance. We can perform a single-parameter fit of the temperature, because we can assume that the abundance matches that of the cluster ($[M/H] = -1.5$; Harris 1996). However, as noted earlier, the cluster hosts sub-populations with distinct metallicities (Marino et al. 2011; Bellini et al. 2017b), while the atmospheric abundances of hot subdwarfs

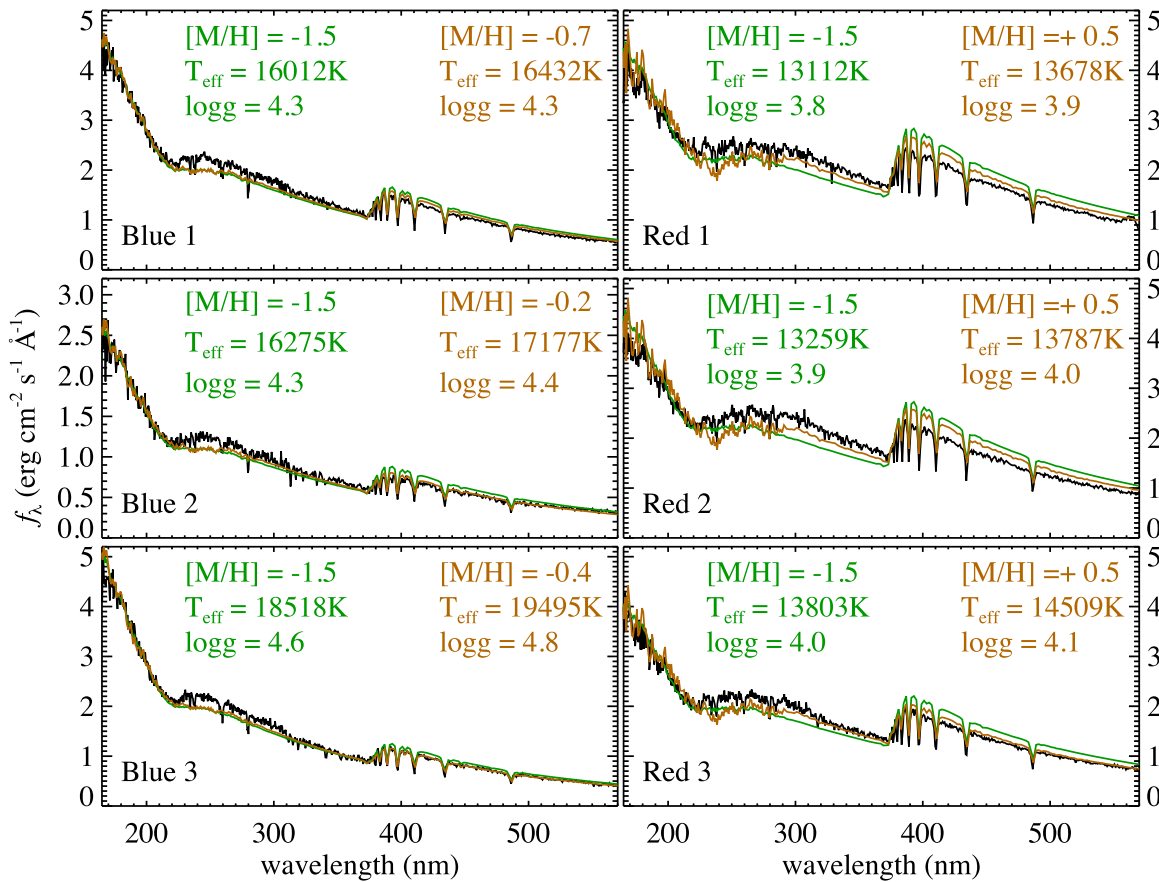


Figure 6. Spectra of our six stars (black curves) compared to the best-fit synthetic spectra (colored curves) from the Castelli & Kurucz (2003) grid. In all of the fits, the effective temperature is allowed to float, and the surface gravity is fixed at the value corresponding to that temperature along the zero-age horizontal branch. The extinction is fixed at $E(B - V) = 0.13$ mag (Bellini et al. 2017b; Milone et al. 2017b). Neither the fits with the metallicity at the mean cluster value ($[M/H] = -1.5$; Harris 1996; green curves) nor the fits with the metallicity allowed to float (labeled; brown curves) are able to match the general shape of the pseudo-continuum and the size of the Balmer jump, although the models with floating metallicity perform somewhat better. Even with the poor fits shown here, the synthetic spectra imply that the red stars are ~ 2000 – 4000 K cooler than the blue stars, and that the red stars have a greater enhancement of atmospheric metallicity due to radiative levitation. Note that the upper metallicity limit in the Castelli & Kurucz (2003) grid is $+0.5$ dex.

show significant variations due to gravitational settling and radiative levitation (Moehler et al. 1999, 2000; Behr 2003; Pace et al. 2006), and we do not expect these subdwarf spectra to reflect the main sequence abundances for any of the cluster’s sub-populations. We assume a foreground extinction of $E(B - V) = 0.13$ mag (Bellini et al. 2017b; Milone et al. 2017b). To fit the model to the data, we define a numerical score as the sum of the squared differences between the observed spectrum and the model spectrum, and then minimize this score using an amoeba simplex algorithm. The effective temperature is allowed to float over the range of 10,000–29,000 K, with initial estimate driven by the photometry (under the assumption of cluster abundance); the surface gravity is set to that of a zero-age HB star at the given effective temperature. The results are shown in Figure 6 (green curves). Although the general shape of each spectrum can be reproduced, the region between the 220 nm extinction bump and the 365 nm Balmer jump is underpredicted in the models, while the size of the Balmer jump is overpredicted in the models. As explained above (Figure 5), for a given effective temperature, the Balmer jump is weaker at higher metallicity, and so it is not surprising that models at cluster metallicity cannot match the Balmer jump in a set of subdwarfs exhibiting significant metal enhancement from radiative levitation. We address this concern by allowing both the temperature and

metallicity to float simultaneously in the fit, using the same amoeba simplex algorithm to minimize the differences between the models and data; the results are also shown in Figure 6 (brown curves). Although these models are an improvement over those at cluster metallicity, they suffer from similar discrepancies. That said, the models imply that the red stars have higher atmospheric metallicities than the blue stars. The fits to the blue stars all favor a metallicity that is enhanced over the cluster value, but is still sub-solar. The fits to the red stars have metallicities consistently limited by the highest metallicity available in the Castelli & Kurucz (2003) grid ($+0.5$ dex).

Given the unusual atmospheric abundances of hot subdwarfs, we next turn to models where the abundances of individual elements can be tuned independently. We use the ATLAS12 and SYNTH codes of Kurucz (2005), which allow elements to be varied independently, but we note that these codes assume a uniform abundance of each element throughout the atmosphere, as opposed to the stratified abundance profiles found in hot subdwarfs (see LeBlanc et al. 2010). The parameter space for such an exploration is large, and the calculations of model atmospheres and synthetic spectra are computationally expensive, but we can approach the problem in a manner that limits the scope. Michaud et al. (2011) calculated stellar evolution models for HB stars at the relevant temperature. Their models for a 14,000 K star (see their Figure 5)

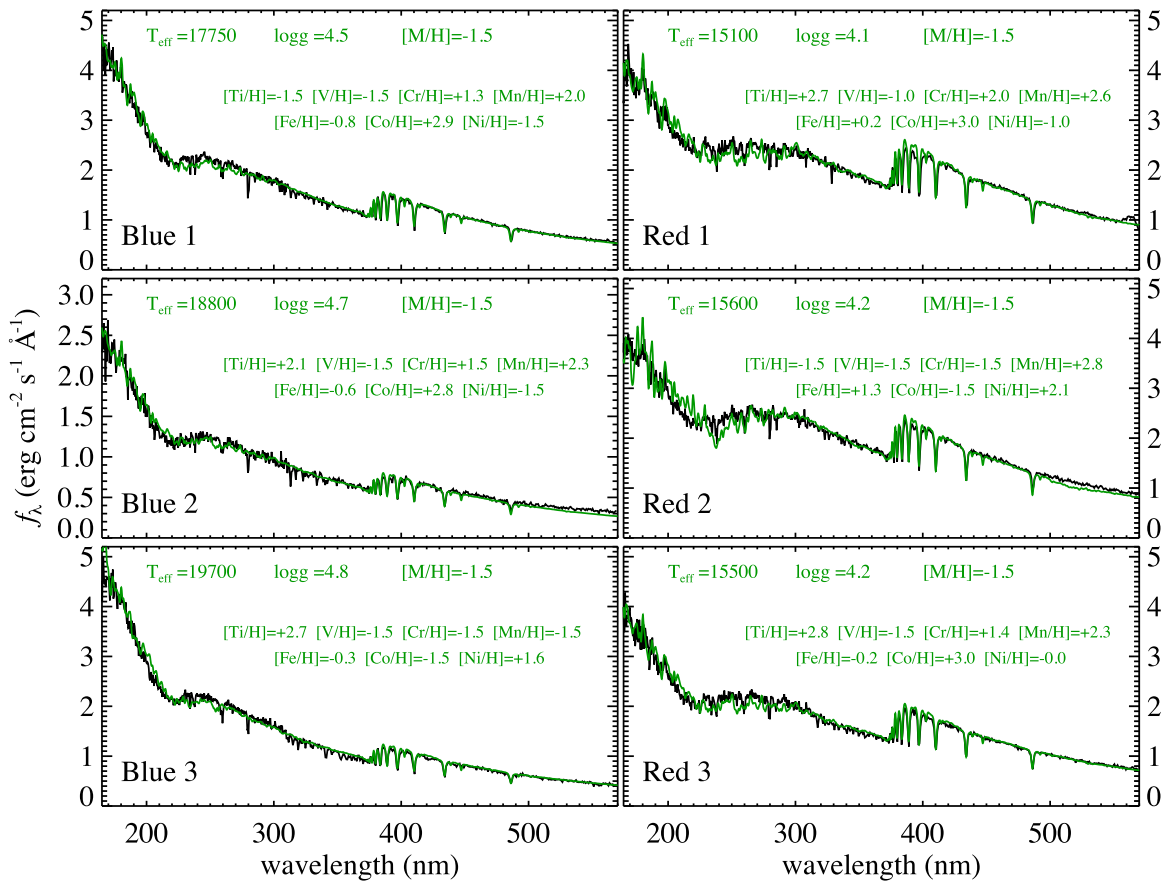


Figure 7. Spectra of our six stars (black curves) compared to the best-fit synthetic spectra (green curves) from ATLAS12 and SYNTH3. In these models, most elements are held at the mean cluster abundance ($[M/H] = -1.5$; Harris 1996), but seven elements (labels) near the Fe peak are allowed to vary up to an enhancement of 4.5 dex over the cluster value, because they can be significantly affected by radiative levitation (Michaud et al. 2011). The best-fit values in each fit (labels) are shown in Figure 8 to ease comparisons. The changes induced on each spectrum by the enhanced atmospheric metallicities are much larger in the red stars than in the blue stars (Figure 9).

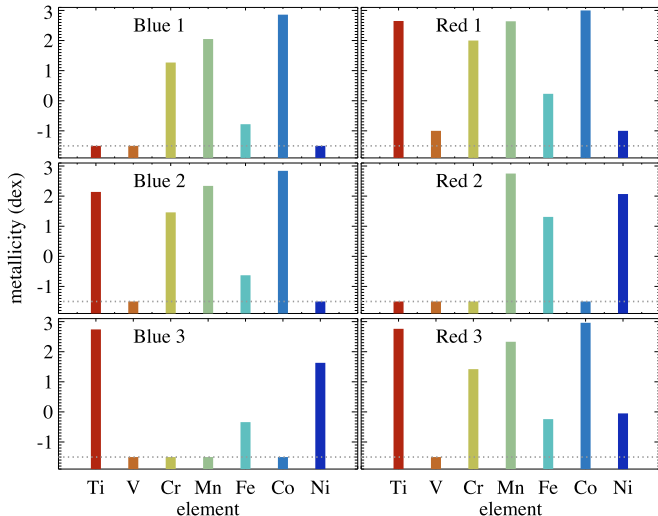


Figure 8. Abundance enhancements (colored bars) in the best-fit model for each star (Figure 7). All of the stars exhibit Fe abundances elevated over the cluster value (dotted line), but the red stars all have higher Fe abundances than the blue stars (albeit with significant star-to-star variation). Ni, Mn, and Cr have a second-order effect on the spectra; these elements tend to exhibit higher enhancements in the red stars than in the blue stars.

imply significant enhancement for the metals Ti through Fe. Of those metals, Fe has the strongest spectral features in our wavelength range, but for completeness we allow variations in

Ti, V, Cr, Mn, Fe, Co, and Ni. Even with this limited set of abundances, it would be prohibitively expensive to iteratively fit our spectra with a procedure that calculated full model atmospheres and synthetic spectra for each abundance step in the fitting process, so we break the fit into two pieces. First, we calculate model atmospheres and synthetic spectra where all but one of the abundances are at the cluster metallicity, and one of these seven abundances is stepped over the cluster value by an enhancement of 0 to +4.5 dex with 0.5 dex steps (i.e., abundances from -1.5 to $+3.0$ dex). This provides an approximation for the spectral features of each individual element as a function of abundance. We then construct a model spectrum from a baseline spectrum (all elements at cluster abundance) and a linear combination of the features from each of our varied elements, determined by comparison to our data with a minimization of differences. Although this linear combination of spectral features is a poor approximation for the true behavior in a stellar atmosphere, the approximation is sufficient for a first estimate. The resulting abundances are then used to construct model atmospheres and associated synthetic spectra, with these spectra serving as the new baseline in the next iteration of fits. The baseline is again modified by a linear combination of spectral features from our seven varied elements, with the results used to calculate the next set of model atmospheres and synthetic spectra. The iterations are continued until the abundance changes for each element are less than 0.1 dex between iterations, at which point the model is considered converged. By the end of

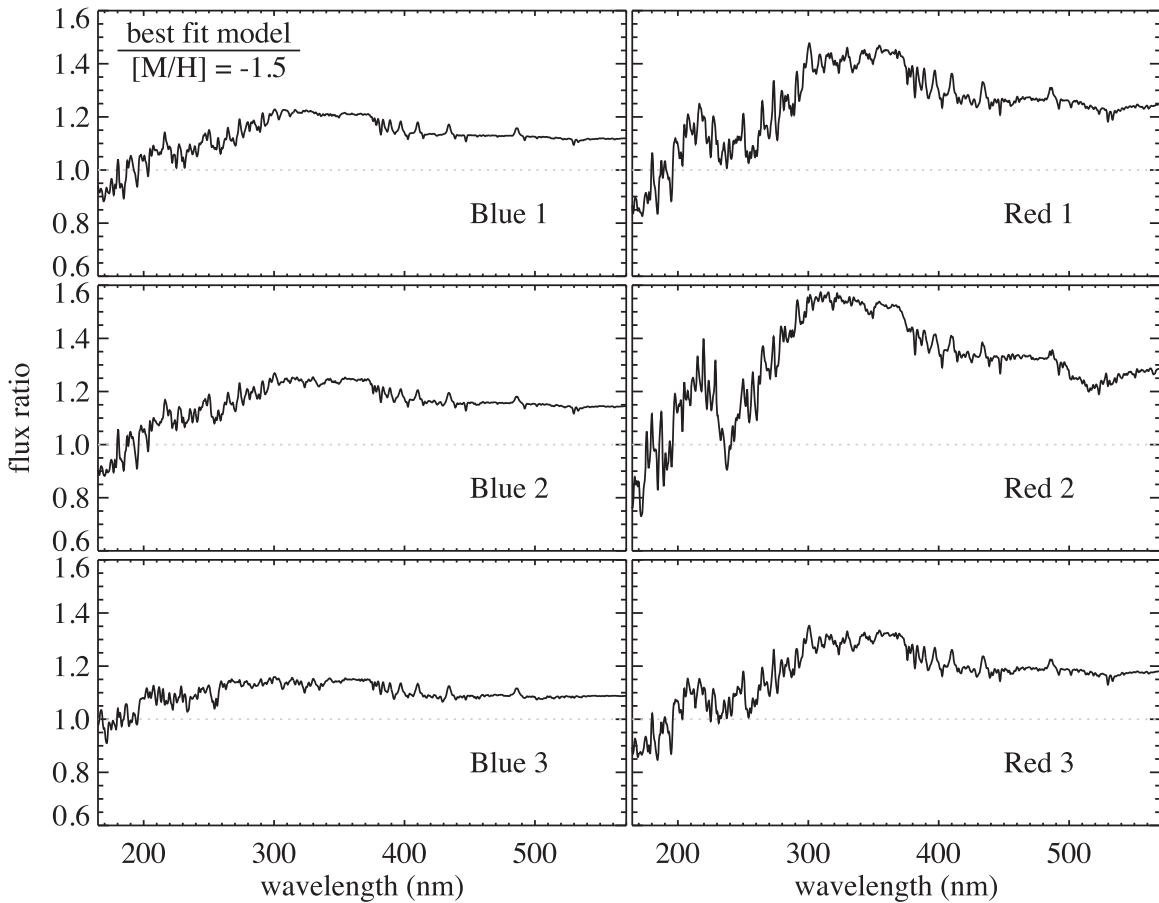


Figure 9. Flux ratio of each best-fit synthetic spectrum (Figure 7) to a synthetic spectrum at the same temperature and gravity, but mean cluster metallicity ($[M/H] = -1.5$). The spectral features in the red stars are all significantly stronger than those in the blue stars, primarily due to the higher Fe abundances and lower effective temperatures in the red stars.

the iterations, the spectral modifications over the baseline, approximated from the library of spectral features for each element, are a small perturbation. After convergence, a final model atmosphere and synthetic spectrum is calculated for each star (Figure 7); the abundance values are plotted in Figure 8 to ease comparisons. The agreement between synthetic and observed spectrum is much improved over the fits with the Castelli & Kurucz (2003) grid, but there are still discrepancies: a residual mismatch in the Balmer jump and deviations at ~ 210 – 260 nm (a region associated with strong Fe features). The effective temperatures implied by our spectroscopic fits are within 600 K of the temperatures implied by the photometry when that photometry is aligned to zero-age HB models (Brown et al. 2016).

For several reasons, it is difficult to provide formal uncertainties for our abundances. Due to the heavy line-blanking in this wavelength range and the low-resolution gratings employed in the observations, none of the elemental abundances in our fits are associated with a well-defined absorption line (or set of lines) in our spectra. Instead, there are regions of the spectra affected to varying degrees by the abundance of a particular element, with no clear region that should be defined to evaluate the fit for each element. Given the overlapping features of these elements, variations in one elemental abundance can be partly compensated by a combination of changes in other elements. Moreover, the processing of the individual raw counts exposures into the final spectrum for each star involves various data reduction packages

that do not propagate the uncertainties in each spectral bin; furthermore, given the finite line spread function and the spatial dithering, the uncertainties in the spectral bins are correlated on the scale of a few bins. Finally, the human and computer labor associated with the production of model atmospheres and synthetic spectra makes it highly impractical to explore the confidence contours in the seven-dimensional parameter space of the abundances varied. However, we can crudely estimate the uncertainties in our abundances by varying individual abundances to trial levels, allowing the other elements to refit and compensate, and inspecting to see if the result is a noticeably worse match to the data. Varying the abundances of Fe, Cr, Mn, and Co implies that they are uncertain at the level of ~ 0.2 dex, while the abundances of Ti and Ni are uncertain at the level of ~ 0.5 dex. The uncertainty in the V abundance is larger than 1 dex (unsurprising, given its weak features). Despite these uncertainties, our analysis indicates that the M-jump is due to a lower atmospheric Fe abundance in the stars hotter than the jump.

There are three clear results in these fits: the blue stars are ~ 2000 – 4000 K hotter than the red stars, all of the stars exhibit abundance enhancements over the cluster value, and the Fe enhancement in the red stars is larger than that in the blue stars. The larger Fe enhancements in the red stars agree with the sense of the M-jump in the color–color plane (Figure 1); our synthetic spectra imply that an increase in Fe abundance by 1 dex will shift the $m_{F275W} - m_{F438W}$ color 0.01 mag redder and increase the C color index by 0.07 mag. The other

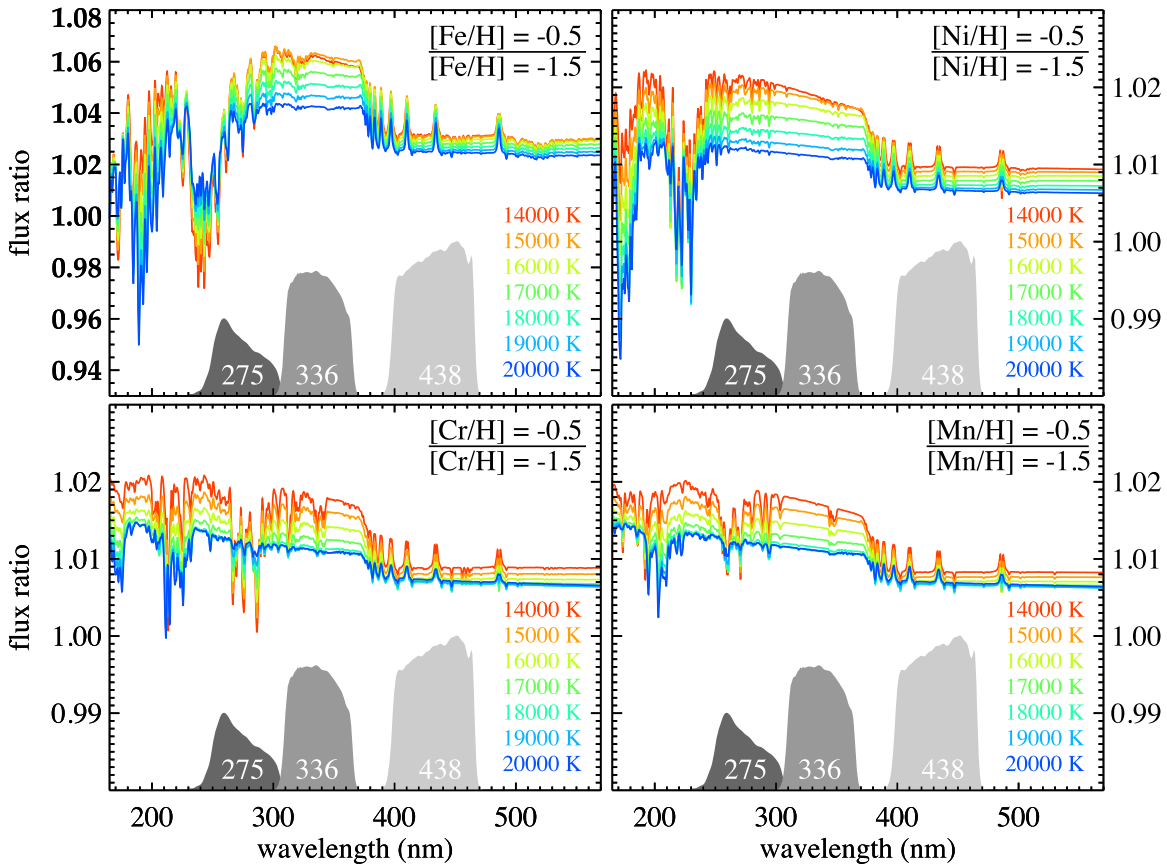


Figure 10. The effect on the spectrum of a hot subdwarf when one of four of the abundances (labeled) is enhanced by 1 dex, as a function of effective temperature. Of the elements varied in our fits, Fe (upper left) has the largest impact in the wavelength range spanned by the F275W, F336W, and F438W filters (bandpasses shown here for reference at arbitrary normalization, and vertically shifted to the bottom of the plot; gray shading), while Cr, Mn, and Ni have a second-order effect (note that the ordinate scale for these three elements is three times smaller than that for Fe). Each curve shows the flux ratio for the synthetic spectrum at enhanced metallicity to the spectrum at mean cluster metallicity, with the colors indicating the effective temperature (labeled). The effect of enhanced metallicity is more significant at the temperatures of the red stars in our sample. For Fe (upper left), the flux falling in the F336W bandpass, relative to that falling in the F275W and F438W bandpasses, is a particularly strong function of effective temperature.

abundances in our fit do not provide a wholly consistent story (Figure 8), but among those that have a secondary influence (Ni, Mn, and Cr), there is a weak trend (with exceptions) for the red stars to have higher enhancements than the blue stars. The remaining elements (Ti, V, and Co) have an even smaller effect in this wavelength range, and there is no clear pattern for these elements. Given this behavior, we also explored models where the abundances of all seven elements were varied in unison; the resulting models agreed less well with the data (as one would expect, given fewer free parameters and the unphysical congruence of abundances), but still implied larger abundance enhancements in the red stars.

Relative to spectra with cluster abundances, the red stars clearly exhibit larger spectral deviations than the blue stars. This can be seen in Figure 9, which shows the ratio of flux in the best-fit synthetic spectrum to that from a model with cluster abundances at the same effective temperature and surface gravity. The larger deviations in the red spectra are driven by the larger Fe abundances (Figure 8) and by the fact that the metals produce stronger spectral features at the lower effective temperatures of the red stars (Figure 10).

4. Discussion

The HB distributions of globular clusters exhibit discontinuities at $\sim 12,000$ K and $\sim 18,000$ K that are remarkably

consistent in effective temperature. The cooler G-jump remains constant despite large changes in many population parameters, with the exception of populations greatly enhanced in helium; the hotter M-jump has exhibited no variation in any cluster observed to date, regardless of population parameters (Brown et al. 2016). Although the G-jump has been attributed to the onset of radiative levitation in hot subdwarfs, the origin of the M-jump has remained unclear. Both features reflect universal phenomena in the atmospheres of hot subdwarfs, and are thus useful fiducials when comparing photometric datasets from distinct populations.

Our spectra of stars straddling the M-jump in ω Cen imply that the feature is due to a change in the atmospheric Fe abundance. While stars on either side of the M-jump exhibit greatly enhanced metal abundances, the enhancement of Fe is stronger for stars falling to the red side of the M-jump, relative to those stars on the blue side of the M-jump. The effect is amplified by the fact that the Fe spectral features are a function of effective temperature, and are stronger for the cooler stars on the red side of the M-jump. The high Fe abundance produces strong spectral features within the F275W bandpass, making the $m_{F275W} - m_{F336W}$ color redder, and weakens the Balmer jump, making $m_{F336W} - m_{F438W}$ color bluer, producing the deviation observed in the color-color diagram of Figure 1.

The same phenomenon appears to be at work in the hot subdwarfs of the Galactic field. Geier et al. (2010; their Figure 1)

show the Fe abundance for field subdwarfs spanning the effective temperatures of both the G-jump and the M-jump. The clear rise in Fe abundance at the G-jump ($\sim 12,000$ K) is the most striking feature in their figure, but there appears to be a drop in Fe abundance when one compares stars on either side of the M-jump ($\sim 18,000$ K); the drop is not significant enough to warrant discussion in their paper, and the dearth of stars near 18,000 K makes it difficult to see if the transition is sharp.

The change in Fe abundance at the M-jump appears to be supported by radiative levitation modeling as well. Michaud et al. (2011) calculated radiative accelerations and associated abundance profiles for metals in the atmospheres of hot subdwarfs spanning 10,700–30,400 K. The Fe surface abundances in their 10,700 and 15,000 K models are significantly higher than that in their 20,000 K model, which is in turn higher than those in their 25,000 and 30,400 K models (see their Figure 8). Like our spectra, their models imply that Fe remains enhanced at temperatures hotter than the M-jump, but that the enhancements are not as strong as those at cooler temperatures. In the Michaud et al. (2011) calculations, the surface abundance enhancements in the various elements do not conform to a regular pattern, given the interplay between depth-dependent radiative acceleration, temperature, and line saturation; for this reason the physical mechanism for the break in the Fe enhancement, responsible for the M-jump, is unclear. The models do not give much insight into the large star-to-star Fe variations in our sample. The radiative levitation timescales are a small fraction of the HB lifetime, such that most HB stars should be observed after the enhancements have stabilized. Brown et al. (2016) also noted that the He II convection zone encroaches upon the surface near the effective temperature of the M-jump, and this encroachment may play a role in the abundance changes producing the M-jump, similar to the role played by convection in the G-jump.

Support for program GO-14759 was provided by NASA through a grant from the Space Telescope Science Institute, which is operated by the Association of Universities for Research in Astronomy, Inc., under NASA contract NAS 5-26555. We are grateful to F. Castelli for making available the model atmosphere (ATLAS12) and synthetic spectra (SYNTHE) codes of R. Kurucz in formats compatible with modern compilers, and for assistance with the installation of these codes. We also thank R. Kurucz for making the codes publicly available. S. Lockwood kindly answered STIS calibration

questions and fixed a bug in the STIS_CTI software. We appreciate useful discussions with A. Aparicio.

ORCID iDs

T. M. Brown  <https://orcid.org/0000-0002-1793-9968>
 S. Cassisi  <https://orcid.org/0000-0001-5870-3735>
 A. Bellini  <https://orcid.org/0000-0003-3858-637X>
 E. Dalessandro  <https://orcid.org/0000-0003-4237-4601>

References

- Anderson, J., & Bedin, L. R. 2010, *PASP*, **122**, 1035
 Behr, B. B. 2003, *ApJS*, **149**, 67
 Bellini, A., Anderson, J., Bedin, L. R., et al. 2017a, *ApJ*, **842**, 6
 Bellini, A., Milone, A. P., Marino, A. F., et al. 2017b, *ApJ*, **844**, 164
 Bostrom, K., & Proffitt, C. 2011, STIS Data Handbook, Version 6.0 (Baltimore: STScI)
 Brown, T. M., Sweigart, A. V., Lanz, T., Landsman, W. B., & Hubeny, I. 2001, *ApJ*, **562**, 368
 Brown, T. M., Cassisi, S., D’Antona, F., et al. 2016, *ApJ*, **822**, 44
 Busso, G., Cassisi, S., Piotto, G., et al. 2007, *A&A*, **474**, 105
 Caloi, V., & D’Antona, F. D. 2007, *A&A*, **463**, 949
 Carretta, E., Gratton, R. G., Clementini, G., & Fusi Pecci, F. 2000, *ApJ*, **533**, 215
 Cassisi, S., Salaris, M., Anderson, J., et al. 2009, *ApJ*, **702**, 1530
 Castelli, F., & Kurucz, R. L. 2003, in IAU Symp. 210, Modeling of Stellar Atmospheres, ed. N. Piskunov, W. W. Weiss, & D. F. Gray (Cambridge: Cambridge Univ. Press), Poster A20
 Catelan, M. 2009, *Ap&SS*, **320**, 261
 D’Cruz, N. L., Dorman, B., Rood, R. T., & O’Connell, R. W. 1996, *ApJ*, **466**, 359
 D’Cruz, N. L., O’Connell, R. W., Rood, R. T., et al. 2000, *ApJ*, **530**, 352
 Geier, S., Heber, U., Edelmann, H., Morales-Rueda, L., & Napiwotzki, R. 2010, *Ap&SS*, **329**, 127
 Grundahl, F., Catelan, M., Landsman, W. B., Stetson, P. B., & Andersen, M. I. 1999, *ApJ*, **524**, 242
 Grundahl, F., VandenBerg, D. A., & Andersen, M. I. 1998, *ApJL*, **500**, L179
 Harris, W. E. 1996, *AJ*, **112**, 1487
 Kurucz, R. L. 2005, *MSAIS*, **8**, 14
 LeBlanc, F., Hui-Bon-Hoa, A., & Khalack, V. R. 2010, *MNRAS*, **409**, 1606
 Marino, A. F., Milone, A. P., Piotto, G., et al. 2011, *ApJ*, **731**, 64
 Michaud, G., Richer, J., & Richard, O. 2011, *A&A*, **529**, A60
 Milone, A. P., Marino, A. F., Bedin, L. R., et al. 2017b, *MNRAS*, **469**, 800
 Milone, A. P., Piotto, G., Renzini, A., et al. 2017a, *MNRAS*, **464**, 3636
 Moehler, S., Sweigart, A. V., Landsman, W. B., & Heber, U. 2000, *A&A*, **360**, 120
 Moehler, S., Sweigart, A. V., Landsman, W. B., Heber, W. B., & Catelan, M. 1999, *A&A*, **346**, L1
 Momany, Y., Bedin, L. R., Cassisi, S., et al. 2004, *A&A*, **420**, 605
 Momany, Y., Piotto, G., Recio-Blanco, A., et al. 2002, *ApJL*, **576**, L65
 Pace, G., Recio-Blanco, A., Piotto, G., & Momany, Y. 2006, *A&A*, **452**, 493
 Piotto, G., Milone, A. P., Bedin, L. R., et al. 2015, *AJ*, **149**, 91